

Topology and stability of a water-soybean-oil swirling flow

Luis Carrión,^{1,2} Miguel A. Herrada,² and Vladimir N. Shtern³

¹*Universidad de las Fuerzas Armadas–ESPE, Avenida General Rumiñahui s/n, Sangolquí, Pichincha 171103, Ecuador*

²*Escuela Superior de Ingenieros, Universidad de Sevilla, Camino de los Descubrimientos s/n, Sevilla, Andalucía 41092, Spain*

³*Shtern Research and Consulting, Houston, Texas 77096, USA*

(Received 15 August 2016; published 22 February 2017)

This paper reveals and explains the flow topology and instability hidden in an experimental study by Tsai *et al.* [Tsai *et al.*, *Phys. Rev. E* **92**, 031002(R) (2015)]. Water and soybean oil fill a sealed vertical cylindrical container. The rotating top disk induces the meridional circulation and swirl of both fluids. The experiment shows a flattop interface shape and vortex breakdown in the oil flow developing as the rotation strength Re_o increases. Our numerical study shows that vortex breakdown occurs in the water flow at $Re_o = 300$ and in the oil flow at $Re_o = 941$. As Re_o increases, the vortex breakdown cell occupies most of the water domain and approaches the interface at Re_o around 600. The rest of the (countercirculating) water separates from the axis as the vortex breakdown cells in the oil and water meet at the interface-axis intersection. This topological transformation of water flow significantly contributes to the development of the flattop shape. It is also shown that the steady axisymmetric flow suffers from shear-layer instability, which emerges in the water domain at $Re_o = 810$.

DOI: [10.1103/PhysRevFluids.2.024702](https://doi.org/10.1103/PhysRevFluids.2.024702)

I. INTRODUCTION

Swirling two-fluid flows have recently attracted the attention of researchers due to applications in aerial vortex bioreactors, a rapidly developing technology [1–3]. These flows have a number of intriguing features of fundamental interest: (i) numerous topological metamorphoses [4], (ii) multiple eddies [5], and (iii) thin circulation layers [6–8]. Fujimoto and Takeda [9] performed an interesting experiment that provided a vivid example of nonlinear physics. They visualized a flow of silicon oil and water driven by the rotating lid in a sealed cylindrical container. As the rotation strength Re_o increased, the interface became significantly deformed, taking shapes named, by the authors, hump, cusp, Mt. Fuji, and bell. Similar results were obtained by Tsai *et al.* [10], who moreover detected vortex breakdown in the upper fluid. However, some important topological features of the lower-fluid motion were uncovered in Refs. [9,10]. These features are related to the vortex breakdown in the water flow.

A topological metamorphosis of a swirling flow, which causes the emergence of a local circulation cell, often referred to as vortex breakdown (VB), has attracted the attention of researchers due to its relevance to delta-wing aircraft, combustion, tornadoes, and other applications [11]. Many hypotheses have been suggested to interpret the VB physics [12]. A recent view is that the swirl-decay mechanism [13] explains why VB occurs and how it can be controlled [14,15].

In contrast to the long-studied history of VB in a single fluid, two-fluid VB flows have only recently been examined. This paper numerically investigates the flow experimentally studied by Tsai *et al.* [10] and reveals that the development of vortex breakdown in the upper fluid is preceded by the development of VB in the lower fluid as the rotation accelerates.

The VB cell emerges near the bottom center, expands upward, and approaches the interface near the axis. This near-axis rise of water causes a significant deformation of the interface. Next, VB occurs in the upper fluid as well. As the water and oil VB cells meet, they expand in the radial direction, forming the flattop shape of the interface.

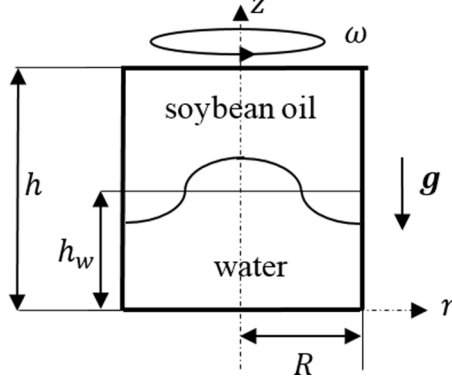


FIG. 1. Schematic of the waterspout model.

This paper shows that the steady axisymmetric flow suffers from shear-layer, time-oscillatory, three-dimensional instability that emerges in the water domain at $\text{Re}_o > 810$. Our stability analysis has been performed using a numerical technique, proving its efficiency for a two-fluid flow with a significantly curved interface [16].

In the following sections, we will formulate the problem (Sec. II), describe the numerical technique (Sec. III), study the topological metamorphoses in water (Sec. IV) and oil (Sec. V) flows, examine the flow stability (Sec. VI), and summarize the results (Sec. VII). The Appendix shows that the obtained results are grid independent.

II. PROBLEM FORMULATION

A. Flow geometry

Figure 1 is a schematic of the problem. The lower part, $0 < z < h_w$, of the cylindrical container of radius R and height h is filled with water; the upper part, $h_w < z < h$, is filled with soybean oil. With no motion, the interface is flat, $z = h_w$ (thin horizontal line in Fig. 1). When the top disk (at $z = h$) rotates with angular velocity ω while the other walls are stationary, the interface becomes deformed, typical of waterspouts, as the curve in Fig. 1 schematically illustrates.

One control parameter is the aspect ratio $H = h/R$, which is fixed here at $H = 2.014$, which corresponds to Fig. 2 of Ref. [10], where $R = 7.2$ cm, $h = 14.5$ cm, and $h_w = 1.5$ cm. The dimensionless height of the interface at rest $H_w = h_w/R = 0.2083$ is also fixed here. To stay consistent with the experiment [10], we vary the Reynolds number $\text{Re}_o = \omega R^2/\nu_o$, characterizing the strength of oil flow; ν_o is the kinematic viscosity of soybean oil. It is also convenient to use $\text{Re} = \omega R^2/\nu_w$; ν_w is the kinematic viscosity of water. Hereafter, subscripts w and o represent water and oil, respectively. To characterize the strength of water flow we use $\text{Re}_w = v_{si}\text{Re}$, where v_{si} is the ratio of the maximal swirl velocity at the interface to ωR .

The other varying parameters are the Froude number $\text{Fr} = \omega^2 R/g = a \text{Re}^2$, which is a centrifugal-to-gravity acceleration ratio, and the Weber number $\text{We} = \rho_w \omega^2 R^3/\sigma = b \text{Re}^2$, characterizing the effect of surface tension σ at the interface. Here $g = 9.81$ m/s² is the gravity acceleration, ρ_w is the water density, $a = \nu_w^2/gR^3$, and $b = \rho_w \nu_w^2/\sigma R$. As the fluids are specified, coefficients a and b are fixed while Re varies.

To stay consistent with Ref. [10], we take $\rho_w = 1000$ kg/m³, $\rho_o = 920$ kg/m³, $\nu_w = 10^{-6}$ m²/s, $\nu_o = 65.22 \times 10^{-6}$ m²/s, and $\sigma = 0.02$ kg/s² [17]. This yields $a = 2.731 \times 10^{-10}$ and $b = 6.944 \times 10^{-7}$. We do not expect a significant effect on σ where the curvature of the interface is small.

B. Governing equations

Using R , ωR , and $\rho_w \omega^2 R^2$ as scales for length, velocity, and pressure, respectively, renders all variables dimensionless. We consider a flow of two viscous incompressible immiscible fluids

governed by the Navier-Stokes equations [18]

$$\frac{1}{r} \frac{\partial(ru)}{\partial r} + \frac{1}{r} \frac{\partial v}{\partial \phi} + \frac{\partial w}{\partial z} = 0, \quad (1)$$

$$\frac{\partial u}{\partial t} + u \frac{\partial u}{\partial r} + \frac{v}{r} \frac{\partial u}{\partial \phi} + w \frac{\partial u}{\partial z} - \frac{v^2}{r} = -\rho_n \frac{\partial p}{\partial r} + \frac{v_n}{\text{Re}} \left(\nabla^2 u - \frac{u}{r^2} - \frac{2}{r^2} \frac{\partial v}{\partial \phi} \right), \quad (2)$$

$$\frac{\partial v}{\partial t} + u \frac{\partial v}{\partial r} + \frac{v}{r} \frac{\partial v}{\partial \phi} + w \frac{\partial v}{\partial z} + \frac{uv}{r} = -\frac{\rho_n}{r} \frac{\partial p}{\partial \phi} + \frac{v_n}{\text{Re}} \left(\nabla^2 v - \frac{v}{r^2} + \frac{2}{r^2} \frac{\partial u}{\partial \phi} \right), \quad (3)$$

$$\frac{\partial w}{\partial t} + u \frac{\partial w}{\partial r} + \frac{v}{r} \frac{\partial w}{\partial \phi} + w \frac{\partial w}{\partial z} = -\rho_n \frac{\partial p}{\partial z} + \frac{v_n}{\text{Re}} \nabla^2 w, \quad (4)$$

where $\nabla^2 \equiv \frac{1}{r} \frac{\partial}{\partial r} \left(r \frac{\partial}{\partial r} \right) + \frac{1}{r^2} \frac{\partial^2}{\partial \phi^2} + \frac{\partial^2}{\partial z^2}$ is the Laplace operator for a scalar field, (u, v, w) are the velocity components in cylindrical coordinates (r, ϕ, z) , t is time, and p is pressure. The coefficients ρ_n and v_n are both equal to 1 at $n = 1$ (in water) while $\rho_n = \rho_w / \rho_o$ and $v_n = v_o / v_w$ at $n = 2$ (in oil).

We denote the list (u, v, w, p) by \mathbf{V} and look for a solution of the system (1)–(4) in the form

$$\mathbf{V} = \mathbf{V}_b(r, z) + \varepsilon \mathbf{V}_d(r, z) e^{(im\phi - i\omega t)} + \text{c.c.}, \quad (5)$$

where subscripts b and d denote the base flow and a disturbance, respectively, c.c. denotes the complex conjugate of the preceding term, $\varepsilon \ll 1$ is an amplitude, the integer m is an azimuthal wave number, and $\omega = \omega_r + i\omega_i$ is a complex number to be found, with frequency ω_r and growth rate of disturbance ω_i . For a decaying (growing) disturbance, ω_i is negative (positive). The equations governing the base flow follow from substituting (5) in the system (1)–(4) and setting $\varepsilon = 0$. The terms of $O(\varepsilon)$ constitute equations governing infinitesimal disturbances.

C. Boundary conditions

Equations (1)–(4) are solved under the following boundary conditions.

(i) Regularity at the axis, where $0 < z < H$ and $r = 0$, yields that (a) $u = v = 0$ and $\partial w / \partial r = 0$ (base flow and $m = 0$ disturbances); (b) $w_d = 0, u_d + v_d = 0$, and $\partial u_d / \partial r = 0$ ($m = 1$ disturbances); and (c) $w_d = u_d = v_d = 0$ ($m > 1$ disturbances).

(ii) No slip at the walls yields that $u = v = w = 0$ at the still disk, where $0 < r < 1$ and $z = 0$, and at the sidewall, where $0 < z < H$ and $r = 1$, and that $u = w = 0$ and $v = r$ at the rotating disk, where $0 < r < 1$ and $z = H$.

(iii) Continuity of all the velocity and tangential stress components at the interface yields that $z = F(r, \phi, t)$. The balance for the normal stresses yields that

$$p_w - p_o = \frac{1}{\text{We}} \nabla \cdot \mathbf{n} - \frac{1}{\text{Re}} \mathbf{n} \cdot (\boldsymbol{\tau}_w - \mu_r \boldsymbol{\tau}_o) \cdot \mathbf{n} - \frac{1}{\text{Fr}} (1 - \rho_r) z, \quad (6)$$

where \mathbf{n} is the unit vector perpendicular to the interface, $\boldsymbol{\tau}_w$ and $\boldsymbol{\tau}_o$ are tensors of the viscous stresses in the water and oil, respectively, and μ_r and ρ_r are the light-to-heavy fluid ratios of the dynamic viscosities and densities, respectively.

(iv) The kinematic equation for the interface shape $z = F(r, \phi, t)$ yields that

$$\frac{\partial F}{\partial t} - w + u \frac{\partial F}{\partial r} + \frac{v}{r} \frac{\partial F}{\partial \phi} = 0 \quad (7)$$

and we look for a solution in the form $z = F_b(r, z) + \varepsilon F_d(r, z) e^{(im\phi - i\omega t)} + \text{c.c.}$

III. NUMERICAL TECHNIQUE

To simulate the nonlinear problem for the axisymmetric base flow and the generalized eigenvalue problem for disturbances, we use a numerical technique that is a variation of that described in detail in Ref. [16]. First, the water and oil regions are mapped onto the standard square domain

($0 \leq \eta_{(w,o)} \leq 1$ and $0 \leq \xi \leq 1$) by means of the coordinate transformations (a) $\eta_w = z/F$ and $\xi = r$ and (b) $\eta_o = (z - F)/(H - F)$ and $\xi = r$ for the water and oil, respectively. Then each variable (velocity, pressure field, and interface shape) and all their spatial and temporal derivatives, which appear in the transformed equations, are composed as a single symbolic vector. For example, for the axial velocity in the water flow, we create a vector having 11 components:

$$\mathbf{x}_w = [w_w, \partial w_w / \partial \eta_w, \partial w_w / \partial \xi, \partial^2 w_w / \partial \eta^2, \partial^2 w_w / \partial \xi^2, \partial^2 w_w / \partial \xi \partial \eta, \partial w_w / \partial \phi, \partial^2 w_w / \partial \phi^2, \partial^2 w_w / \partial \phi \partial \xi, \partial^2 w_w / \partial \phi \partial \eta, \partial w_w / \partial t].$$

The next step is to use a symbolic toolbox to calculate the analytical Jacobian matrices of all the equations with respect to all the symbolic vectors. Using these analytical Jacobian matrices, we generate functions, which then are evaluated point by point in the square domains. In this procedure, we used the MATLAB procedure *matlabFunction* to convert the symbolic Jacobian matrices into MATLAB functions.

Then we carry out the spatial and temporal discretization of the problem. The water and oil domains are discretized using a set of n_w and n_o Chebychev spectral collocation points in the axial direction (along the η_w and ξ_o axes, respectively) [19]. The water and oil domains are discretized using a set of n_ξ Chebychev spectral collocation points in the radial direction ξ . The second-order backward finite differences are used to compute the time derivatives for the base flow. Since the base flow is axisymmetric, all the azimuthal derivatives are set to zero. For disturbances, we obtain the temporal and azimuthal derivatives using the representation (5). This helps overcome the technical difficulty of linearizing the relation (6) for the linear stability study of two-fluid flows.

The final step is to set up the numerical matrices, allowing us to solve the problem by using a Newton procedure for the base steady flow and by solving a generalized eigenvalue problem for disturbances. Details of this procedure are described in Ref. [16].

To summarize, the numeric procedure includes the mapping of water and oil regions, the proper spatial and temporal discretization creating the discrete Jacobian matrix of the Newton procedure for the base flow, and two more matrices for the generalized eigenvalue problem for disturbances. For the base flow, we get the final steady solution through an unsteady process. Starting from rest and selecting a time step dt , the solution is advanced through time until a steady state is reached. Since the nonlinear procedure used to compute the base flow is fully implicit, a sufficiently large dt can be taken to quickly reach the steady solution. Once the base flow is computed and given an azimuthal wave number m , we use MATLAB subroutine *eigs* to calculate the eigenvalues ω for the system of discrete linear equations.

Most of the simulations presented here are done using $n_w = 60$ and $n_o = 25$ in the axial direction and $n_\xi = 40$ in the radial direction (standard grid), but due to their small circulation regions, some simulations for flows at large Re are performed with finer grids. The larger n_w compared with n_o is used because the oil viscosity is significantly larger than the water viscosity.

Since the Chebyshev grid points concentrate near the interface from both sides, the approach is adequate to resolve thin circulation layers located near the interface, even at moderate values of n_w , n_o , and n_ξ . The Chebyshev grid points also concentrate near the axis and all walls, helping to resolve the small flow cells located near them. To analyze the flow topology, we use the Stokes stream function Ψ , $w = r^{-1} \partial \Psi / \partial r$, and $u = -r^{-1} \partial \Psi / \partial z$ and plot streamlines of the meridional motion, i.e., contours $\Psi = \text{const}$.

IV. TOPOLOGICAL METAMORPHOSES OF WATER FLOW

A. Moffatt and near-interface eddies

It is instructive to start with a creeping flow and to gradually increase the Reynolds number characterizing the strength of oil flow Re_o . Figures 2(a)–2(c) depict streamlines at $Re_o = 1, 40$, and 60, respectively. The bold red curve denotes the interface. The clockwise (counterclockwise) circulation is shown hereafter by light (dark) blue contours. Figure 2(a) depicts the pattern of the

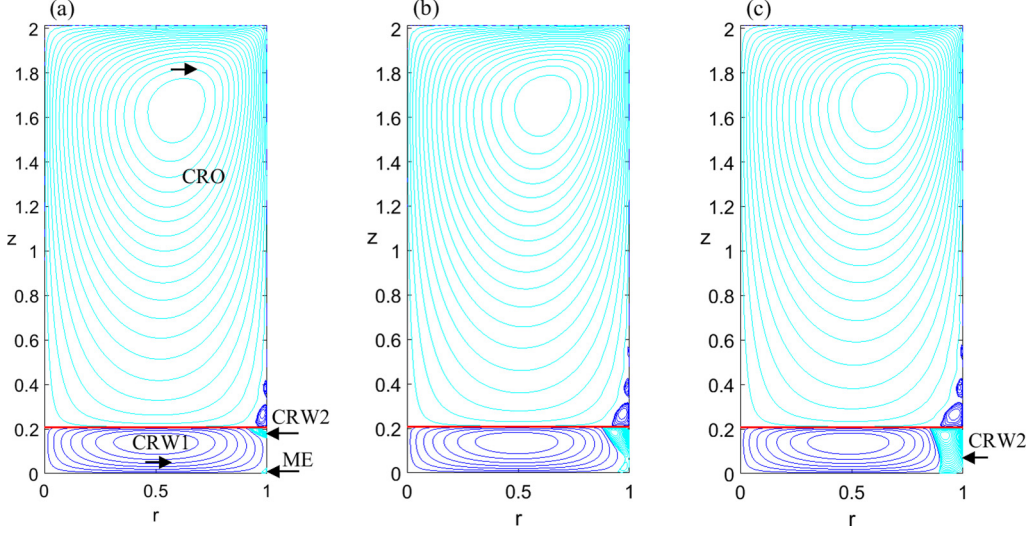


FIG. 2. Patterns of meridional motion at (a) $Re_o = 1$, (b) $Re_o = 40$, and (c) $Re_o = 60$.

creeping flow. The rotating lid pushes the upper fluid to the periphery near the lid and thus drives the clockwise circulation in the circulation region of oil (CRO). Near the interface, the oil moves toward the container axis.

The water flow is driven by two factors, (i) swirl and (ii) meridional velocities at the interface, both provided by the oil motion. Factors (i) and (ii) push the water in opposite directions: The swirl (meridional) velocity tends to drive the clockwise (counterclockwise) meridional circulation. For $Re_o = 1$, the swirl velocity at the interface is very small, as discussed in more detail below. Therefore, factor (ii) dominates over (i) and drives the bulk counterclockwise circulation marked as CRW1 in Fig. 2(a), where W denotes the water.

This circulation induces the Moffatt eddies near the sidewall-bottom intersection, as Fig. 2(a) illustrates. Moffatt [20] revealed that a flow in a corner (between two inclined planes with a sufficiently small angle) has an infinite set of eddies whose strength and scale diminish to zero as the edge is approached. Since the outermost eddy size is small compared with the cylinder radius [see ME in Fig. 2(a)], the sidewall can be approximated by a tangential plane, thus reducing the cylindrical geometry to the corner between orthogonal planes. The corner angle of 90° is sufficiently small for the Moffatt eddies to occur [20]. Our numerical grid only resolves the outermost Moffatt eddy, denoted by ME in Fig. 2(a).

The Moffatt eddies also develop near the interface-sidewall intersection [21]. Our numerical grid only resolves the outermost near-interface eddy in water, marked as CRW2 in Fig. 2(a). CRW2 drives the small counterclockwise cell right above CRW2 in the oil flow. In turn, this cell induces one, in Fig. 2(a), or two, in Figs. 2(b) and 2(c), near-sidewall small eddies. As Re_o increases, ME and CRW2 expand in the z direction, touch each other, as Fig. 2(b) illustrates, and merge. The merged cell is denoted again by CRW2 in Fig. 2(c).

B. Vortex breakdown in water flow

The water moves upward in the bulk flow near the sidewall and thus blocks the downward transfer of the angular momentum from the interface. The angular momentum is transported toward the axis along the interface and then downward near the axis in the water domain. Therefore, the swirl effect is the strongest near the axis-bottom intersection where the VB cell emerges as Re_o increases and factor (i) strengthens. The VB cell is denoted by CRW3 in Fig. 3(c).

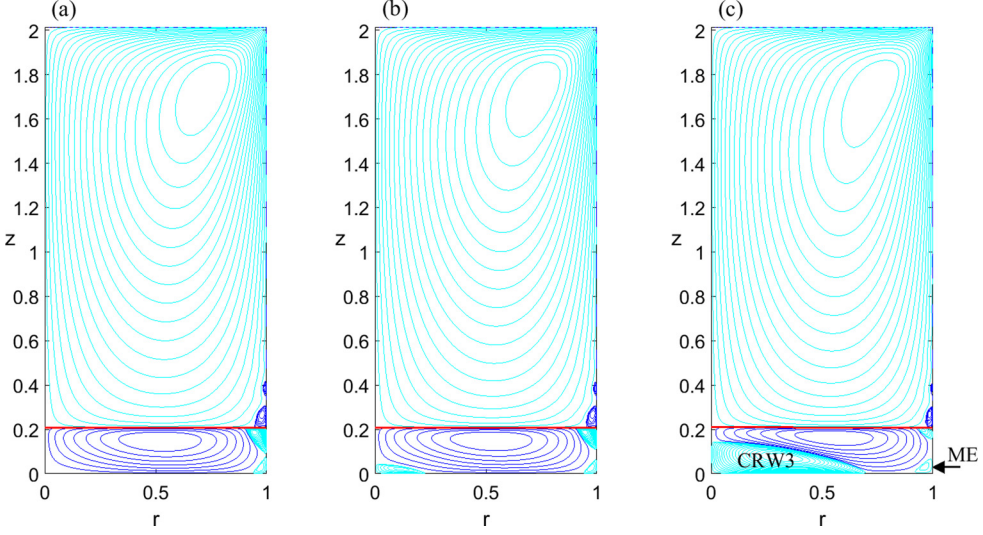


FIG. 3. Patterns of meridional motion at (a) $Re_o = 300$, (b) $Re_o = 310$, and (c) $Re_o = 370$ show formation of the VB cell CRW3 in water.

Figure 4 shows the distribution of velocity w at the axis in water at $Re_o = 250$ (dashed curve), 300 (solid curve), and 305 (dotted curve). To better observe the small-magnitude velocity near the bottom, $z = 0$, Fig. 4 plots $w^{1/3}$. As Re_o increases, the $w > 0$ range that corresponds to the VB water cell appears. Interpolating $\partial w / \partial z$ at $r = z = 0$ as a function of Re_o yields that CRW3 emerges at $Re_o \approx 300$. Figure 5 depicts the dependence of the maximal value of swirl velocity at the interface v_{si} on Re_o . This dependence helps explain why the VB in water occurs at $Re_o = 300$. At small Re_o , the water rotation is very weak, $v_{si} = 0.0015$. The v_{si} value starts to significantly grow for $Re_o > 100$ and becomes nearly 0.07 at $Re_o = 300$, which corresponds to the inflection point of the curve in Fig. 5.

The Reynolds number, based on v_{si} and the water viscosity ν_w , is $Re_w = 1370$ at $Re_o = 300$, i.e., the water rotates sufficiently fast for the nonlinear terms to become important in Eqs. (2)–(4). As the rotating fluid meets a normal wall, the secondary flow develops [22]. This flow radially converges to the rotation axis near the wall and goes away from the wall near the axis. The driving mechanism for the secondary flow is the radial gradient of pressure. It develops away from the wall to balance the centrifugal force: $\partial p / \partial r = \rho v^2 / r$. Near the wall, $\partial p / \partial r$ is not balanced by the centrifugal force

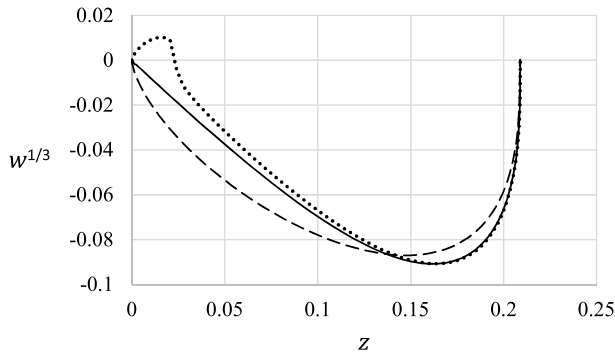


FIG. 4. Distribution of velocity w at the axis in the water domain at $Re_o = 250$ (dashed curve), $Re_o = 300$ (solid curve), and $Re_o = 305$ (dotted curve).

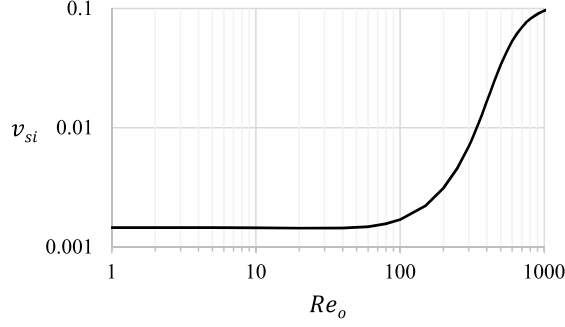


FIG. 5. Dependence of maximal swirl velocity at the interface v_{si} on the Reynolds number.

(because it has the second-order zero since $v = 0$ at the wall) and pushes the fluid radially inward. This tornadolike secondary motion becomes sufficiently strong to overcome the counterclockwise circulation of water near the axis-bottom intersection at $Re_o = 300$.

C. Formation of thin counterclockwise circulation layer in water

As Re_o further increases, the vortex breakdown cell CRW3 and the outermost Moffatt eddy ME, shown in Fig. 3(c), merge and form the clockwise circulation, denoted again by CRW3 in Fig. 6(a). The counterclockwise circulation CRW1 separates from the bottom, as Fig. 6(a) illustrates at $Re_o = 400$, and becomes a thin layer, as Fig. 6(b) illustrates at $Re_o = 600$. The z extent of CRW1 at the axis, $r = 0$, becomes very small: 0.007 at $Re_o = 600$.

D. Growth of the interface height at the axis

This reduction results in the significant rise of the interface near the axis, driven by the water upflow in region CRW3, as Fig. 6(b) illustrates. Figure 7 depicts this trend in more detail by showing the dependence of the interface height at the axis, z_i , on Re_o .

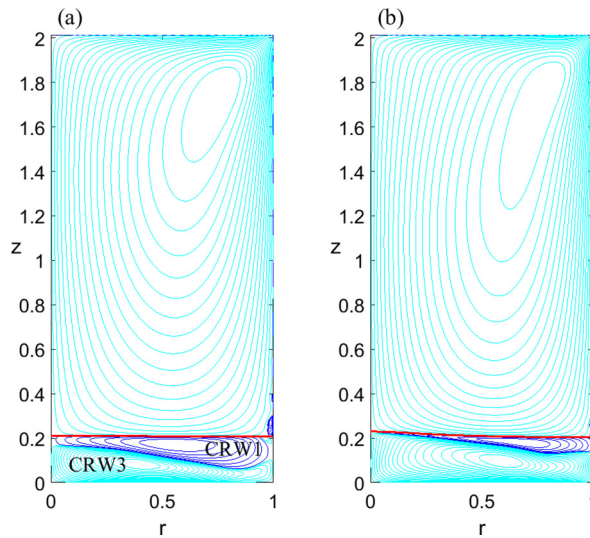


FIG. 6. Patterns of meridional motion at (a) $Re_o = 400$ and (b) $Re_o = 600$ show formation of a thin counterclockwise circulation layer in water.

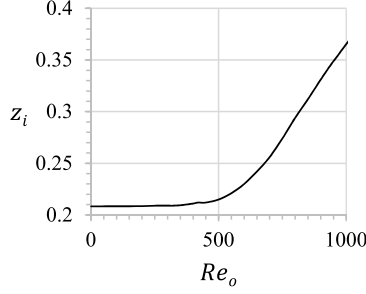


FIG. 7. Dependence of interface height at the axis z_i on the rotation speed Re_o .

E. Formation of a bulge in the counterclockwise layer

The interface rises in the axis vicinity but remains nearly flat for $r > 0.3$, as Fig. 8 illustrates. This causes an intriguing effect: the formation of a bulge in the counterclockwise water circulation. At $Re_o = 700$, the water motion is pretty fast, since $Re_w = 3742$. A strong jet forms near the interface. The interface peak at the axis makes this jet inclined downward. The inertia force separates the jet from the interface, where the interface becomes nearly flat, resulting in the bulge observed in Fig. 8(b). The bulge divides the clockwise water circulation in the near-axis and near-sidewall parts in Fig. 8(b). Figure 8(b) also shows that oil streamlines have a swelling near the axis for z close to 1.2. This swelling is a precursor of vortex breakdown in the oil flow discussed below.

V. VORTEX BREAKDOWN IN OIL FLOW

A. Accumulation of swirl near the axis-interface intersection

Figure 8 indicates the formation of a jet radially converging toward the axis near the interface in the oil flow. This intensifies the swirl near the axis-interface intersection. The dashed ($Re_o = 700$) and solid ($Re_o = 850$) curves in Fig. 9 show that the swirl velocity v at the interface increases with Re_o and its peak location shifts closer to the axis. This significantly increases the centrifugal

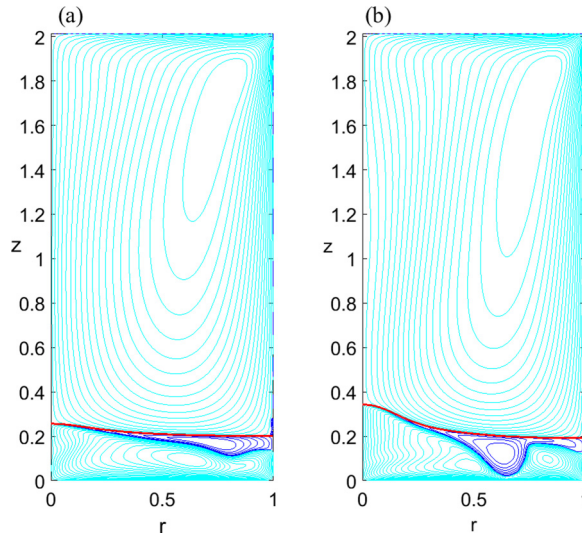


FIG. 8. Patterns of meridional motion at (a) $Re_o = 700$ and (b) $Re_o = 933$ show formation of a bulge in a counterclockwise circulation layer in water.

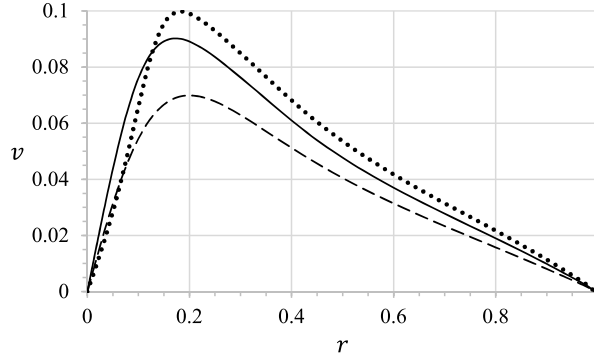


FIG. 9. Distribution of swirl velocity at the interface at $Re_o = 700$ (dashed curve), $Re_o = 850$ (solid curve), and $Re_o = 1082$ (dotted curve).

acceleration v^2/r and consequently the radial gradient of pressure, resulting in a local pressure minimum near the axis-interface intersection.

B. Distribution of velocity at the axis in the oil flow

The reduced pressure sucks the downstream oil, decelerating the upward oil motion near the axis. Figure 10 illustrates this trend by depicting the distribution of oil velocity at the axis at the Re_o values shown near the curves. A local minimum of w forms, its location approaches the interface, and its value decreases as Re_o increases.

C. Emergence and development of vortex breakdown in the oil flow

Interpolation of the local minimal w value as a function of Re_o yields that vortex breakdown in oil occurs at $Re_o = 941$. The VB cell in oil emerges at the axis near $z = 1$ and then extends in both the radial and axial directions. Interpolating $\partial w / \partial z$ at the interface as a function of Re_o yields that the vortex breakdown cell reaches the interface at $Re_o = 1000$. Figures 11(a) and 11(b) depict the vortex breakdown patterns at $Re_o = 966$ and 1033, respectively.

As the VB oil cell reaches the interface, it meets the VB water cell. Next the stagnation saddle point S separates from the axis, as Fig. 11(b) illustrates. The counterclockwise circulation region in water detaches from the axis as well. All bulk flow regions meet at S for $Re_o > 1000$. The vortex breakdown patterns in the oil flow, depicted in Fig. 11, agree with the experimental vortex breakdown patterns shown in Figs. 2(b) and 2(b*c) of Ref. [10].

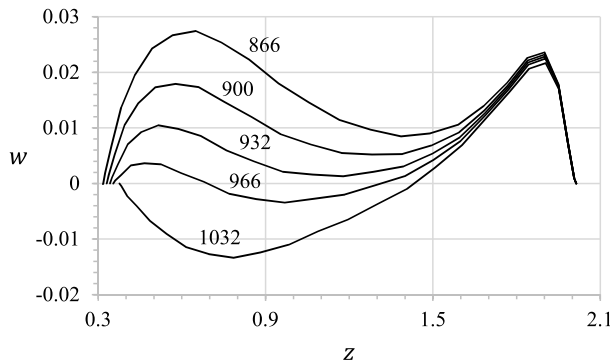


FIG. 10. Distribution of oil velocity at the axis at Re_o values shown near the curves.

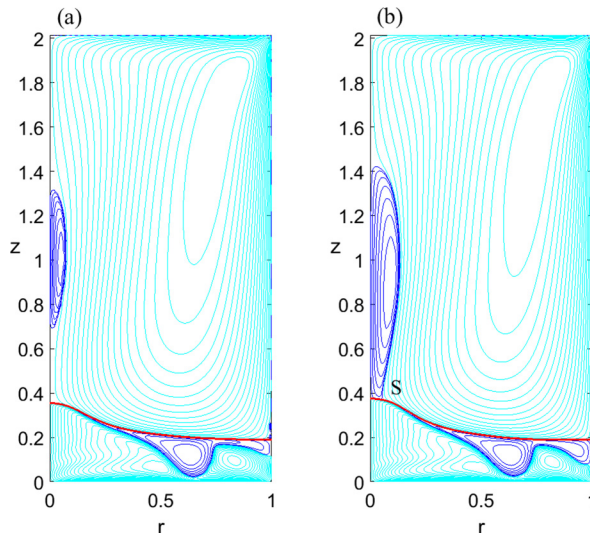


FIG. 11. Patterns of meridional motion at (a) $Re_o = 966$ and (b) $Re_o = 1033$ show the vortex breakdown cell in oil.

In contrast, the striking pattern of the water flow is not resolved in Ref. [10]. An advantage of numerical simulations is that they help investigate a flow in fine detail. In particular, our study reveals the complicated structure of the water flow, which plays an important role in the development of the flattop shape (referred to as the Mt. Fuji shape in Ref. [9]) of the oil-water interface.

VI. STABILITY ANALYSIS

Here we study the stability of the oil-water flow to infinitesimal disturbances. For the Reynolds number exceeding its critical value, growing disturbances can saturate to small amplitudes, according to the experimental results [9,10], but this saturation is not described here. We refer the reader to Refs. [16,23] for technical details of the stability study and discuss the results summarized in Table I. It lists the characteristics corresponding to the marginal disturbances at the azimuthal wave number $m = 1, 2, 3$, and 4. The marginal disturbances are neutral, $\omega_i = 0$, corresponding to Re_o at which all other eigenvalues have $\omega_i < 0$ for a prescribed m .

The critical disturbance is the marginal one, corresponding to the minimal Re_o for all m . The critical characteristics are shown bold in Table I. The Reynolds number of the water flow Re_w is based on the water viscosity ν_w and the maximal azimuthal velocity at the interface, whose dimensionless value v_{si} is also presented in Table I. The minimal meridional tangential velocity at the interface v_{tm} is negative in Table I because it is directed toward the axis as Fig. 12(a) illustrates. The location of the peak marginal-disturbance squared velocity modulus E_d corresponds to $r = r_m$ and $z = z_m$, shown in the last two columns of Table I. Here $E_d = \langle |u_d|^2 + |v_d|^2 + |w_d|^2 \rangle$, where the angular

TABLE I. Marginal ($\omega_i = 0$) and critical (bold) stability characteristics.

m	ω_r	Re_o	Re_w	v_{si}	v_{tm}	r_m	z_m
1	0.073	854	4829	0.0827	-0.0342	0	0.0261
2	0.0097	810	4371	0.0867	-0.0315	0.714	0.153
3	0.0241	842	4689	0.0854	-0.0329	0.874	0.106
4	0.0388	849	4758	0.0859	-0.0332	0.874	0.111

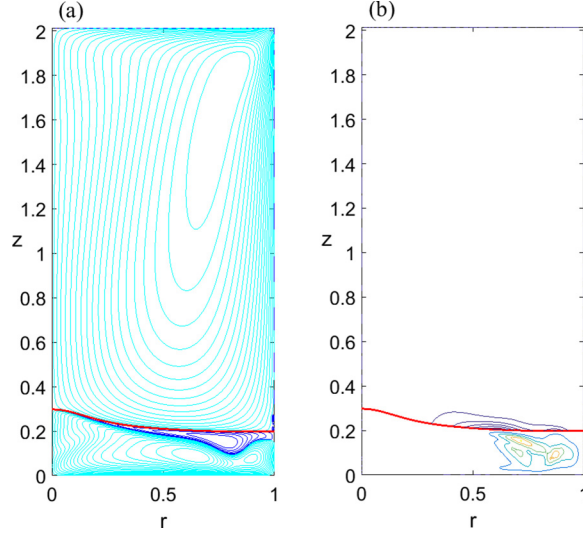


FIG. 12. (a) Meridional motion and (b) contours of constant energy of critical disturbances at $\text{Re}_o = 810$ and $m = 2$.

brackets denote averaging with respect to time and the azimuthal angle. Further, E_d is normalized by its maximal value in the entire domain. A distribution of E_d indicates where the disturbance magnitude is maximal, indicating where it most production occurs.

Other m values not presented in Table I correspond to larger Re_o . Thus, the flow becomes unstable with respect to time-oscillating three-dimensional disturbances for $\text{Re}_o > 810$.

Figure 12 depicts streamlines of meridional motion [Fig. 12(a)] and contours $E_d = \text{const}$ at the critical $\text{Re}_o = 810$ and $m = 2$ [Fig. 12(b)] and reveals that E_d is focused in the water domain. Figure 13 illustrates this feature in more detail by depicting the z distribution of base-flow radial velocity v_r (solid curves) and disturbance energy E_d (dashed curves) at $r = r_m = 0.714$ (see Table I). For convenient observation in one figure, v_r is normalized by its maximal value in Fig. 13.

The peak of radial velocity near $z = 2$ in Fig. 13(a) corresponds to the jetlike oil flow near the rotating disk where the von Kármán boundary layer [24] develops, which is clearly shown in Fig. 12(a). The swirl and radial velocity magnitudes are significantly smaller near the interface (see

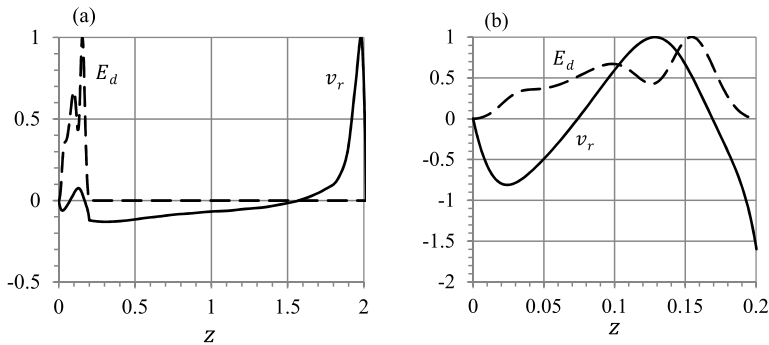


FIG. 13. (a) Plot of the z distributions of base-flow radial velocity v_r and critical disturbance energy E_d at $r = 0.714$, $\text{Re}_o = 810$, and $m = 2$. (b) Close-up of (a) for the water flow only.

the fifth and sixth columns in Table I). The large value of $Re_w = 4371$ is due to the water viscosity being smaller by two orders of magnitude compared with the oil viscosity.

For the same reason, the disturbance energy in the oil is negligible compared with that in the water, as Fig. 13(a) illustrates. This explains why in experiment [10], where the oil flow was only visualized, no effect was observed of time-oscillating three-dimensional water motion.

Figure 13(b) is a close-up of Fig. 13(a) showing the water-flow features in more detail. The v_r profile depicts a well-developed counterflow with inflection points, one near $z = 0.08$ and the other at the interface, which is likely responsible for the instability found. The two local maxima of E_d , observed in Fig. 12(b), are located in the two circulation water cells, observed in Fig. 12(a). This supports our view that the instability is of shear-layer type.

VII. CONCLUSION

This numerical study reveals the flow topology and instability hidden in the experimental study [10]. It shows that vortex breakdown occurs in the water flow at the Reynolds number $Re_o = 300$, which is significantly smaller than $Re_o = 941$, corresponding to vortex breakdown in the oil flow.

For small Re_o , the bulk oil meridional circulation is clockwise and the water circulation is counterclockwise except in small Moffatt eddies occurring near the sidewall-bottom and sidewall-interface intersections [Fig. 2(a)]. The water-flow vortex breakdown causes the emergence of clockwise circulation near the bottom center (Fig. 3). As Re_o increases, this circulation occupies most of water domain and approaches the interface at Re_o around 600 (Fig. 6). The counterclockwise water circulation shrinks into a thin layer attached to the entire interface.

The near-axis uprising water flow, emerging due to vortex breakdown, pushes the interface up and thus causes its significant deformation near the container axis (Fig. 8).

At $Re_o = 810$, the flow becomes unstable with respect to time-oscillating three-dimensional disturbances with the azimuthal wave number $m = 2$ (Table I). The disturbance energy is focused in the water flow near $r_m = 0.714$ and $z_m = 0.153$ where two cells of clockwise circulation develop (Fig. 12). The disturbance energy drastically diminishes in the oil flow (Fig. 13). For the Reynolds number exceeding its critical value, growing disturbances can saturate to small amplitudes, according to the experimental results [9,10], but this saturation is not described here.

As the Reynolds number further increases, the vortex breakdown cells in oil and water meet at the interface-axis intersection at $Re_o = 1000$ and expand in the radial direction, forming the flattop interface shape. Therefore, the observed topological transformations of water flow significantly contribute to the development of flattop shape (Fig. 11).

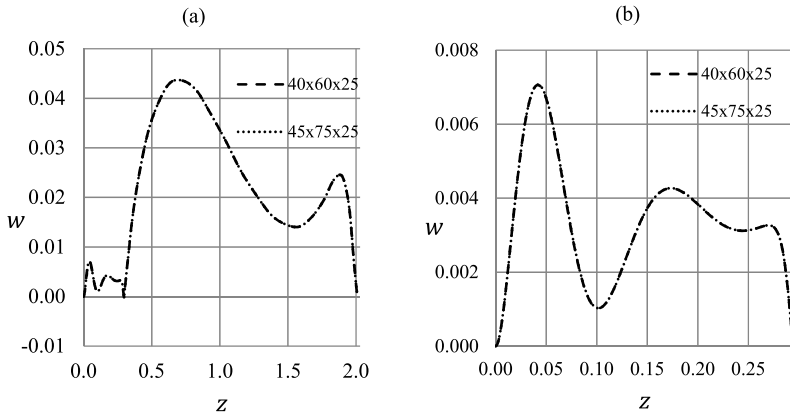


FIG. 14. (a) Velocity on the axis at $Re_o = 810$ calculated with standard (dashed curve) and improved (dotted curve) meshes. (b) Close-up of (a) in the water region $0 < z < 0.30$.

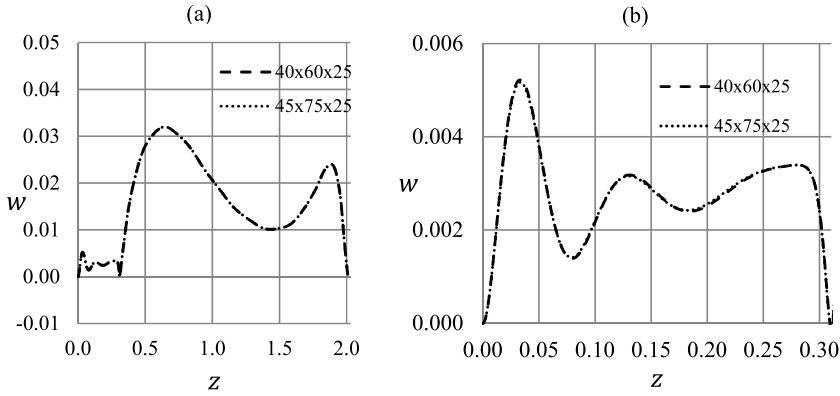


FIG. 15. (a) Velocity on the axis at $Re_o = 850$ calculated with standard (dashed curve) and improved (dotted curve) meshes. (b) Close-up of (a) in the water region $0 < z < 0.30$.

It seems that the water pulsations do not significantly affect the oil motion even for Re remarkably larger than 810 since the unsteadiness was not recognized in the experiment [10]. Figure 13(a) supports this conjecture, indicating that E_d is concentrated in the water domain and is drastically reduced in the oil flow. Our conjecture is that the pulsations are damped by the oil viscosity, which is 65 times the water viscosity. This explains why our results describing the topology transformations of oil flow agree with experiment. The numerical analysis of unsteady flow states requires a more powerful numerical technique and further study.

ACKNOWLEDGMENT

Partial support from the Ministry of Science and Education (Spain) through Grant No. DPI2010-21103 and Junta de Andalucía (Spain) through Grant No. P08-TEP-04128 is gratefully acknowledged.

APPENDIX: CHECKUP OF GRID CONVERGENCE

Figures 14 and 15 illustrate how the velocity distribution on the axis, $w(z)$ at $r = 0$, depends on the number of grid points for large Re values: at $Re_o = 810$ and 850 , respectively. The velocity on the axis is especially susceptible to grid variations because $w(z)$ at $r = 0$ is small, $|w| < 0.05$, compared with the maximal velocity at the rotating disk, which is 1, and with the maximal magnitudes of swirl and meridional velocities at the interface.

The dashed curves correspond to the standard mesh ($n_{\eta w} = 60$, $n_{\eta o} = 25$, and $n_{\xi} = 40$) and the dotted curves correspond to the improved mesh ($n_{\eta w} = 75$, $n_{\eta o} = 25$, and $n_{\xi} = 45$) in Figs. 14 and 15.

The standard-grid and improved-grid results are quite similar in Figs. 14(b) and 15(b), where the velocity is very small ($|w| < 0.007$) compared with the maximal magnitudes of swirl and meridional velocities at the interface. This checkup shows that the results reported in the present paper are sufficiently precise and grid converged.

[1] K. Y. S. Liow, G. A. Thouas, B. T. Tan, M. C. Thompson, and K. Hourigan, in *Modelling the transport of momentum and oxygen in an aerial-disk driven bioreactor used for animal tissue or cell culture*, edited by

- C. T. Lim and J. C. H. Goh, *Proceedings of the 13th International Conference on Biomedical Engineering* (Springer, Berlin, 2008), Vol. 23, pp. 1672–1675.
- [2] K. Y. S. Liow, B. T. Tan, G. Thouas, and M. C. Thompson, CFD Modeling of the steady-state momentum and oxygen transport in a bioreactor that is driven by an aerial rotating disk, *Mod. Phys. Lett. B* **23**, 121 (2009).
- [3] D. Lo Jacono, M. Nazarinia, and M. Brøns, Experimental vortex breakdown topology in a cylinder with a free surface, *Phys. Fluids* **21**, 111704 (2009).
- [4] A. Balci, M. Brons, M. A. Herrada, and V. N. Shtern, Vortex breakdown in a truncated conical bioreactor, *Fluid Dyn. Res.* **47**, 065503 (2015).
- [5] M. A. Herrada and V. N. Shtern, Patterns of a creeping water-spout flow, *J. Fluid Mech.* **744**, 65 (2014).
- [6] M. A. Herrada, V. N. Shtern, and J. Lopez-Herrera, Vortex breakdown in a water-spout flow, *Phys. Fluids* **25**, 093604 (2013).
- [7] P. T. Brady, M. Herrman, and J. M. Lopez, Two-fluid confined flow in a cylinder driven by a rotating end wall, *Phys. Rev. E* **85**, 016308 (2012).
- [8] P. T. Brady, M. Herrman, and J. M. Lopez, Addendum to “Two-fluid confined flow in a cylinder driven by a rotating endwall”, *Phys. Rev. E* **85**, 067301 (2012).
- [9] S. Fujimoto and Y. Takeda, Topology changes of the interface between two immiscible liquid layers by a rotating lid, *Phys. Rev. E* **80**, 015304(R) (2009).
- [10] J.-C. Tsai, C.-Y. Tao, Y.-C. Sun, C.-Y. Lai, K.-H. Huang, W.-T. Juan, and J.-R. Huang, Vortex-induced morphology on a two-fluid interface and the transitions, *Phys. Rev. E* **92**, 031002(R) (2015).
- [11] V. N. Shtern, *Counterflows* (Cambridge University Press, Cambridge, 2012).
- [12] V. N. Shtern and F. Hussain, Collapse, symmetry breaking, and hysteresis in swirling flows, *Annu. Rev. Fluid Mech.* **31**, 537 (1999).
- [13] V. N. Shtern and A. A. Borissov, Nature of counterflow and circulation in vortex separators, *Phys. Fluids* **22**, 083601 (2010).
- [14] V. N. Shtern, M. M. Torregrosa, and M. A. Herrada, Effect of swirl decay on vortex breakdown in a confined steady axisymmetric flow, *Phys. Fluids* **24**, 043601 (2012).
- [15] M. A. Herrada, V. N. Shtern, and M. M. Torregrosa, The instability nature of the Vogel-Escudier flow, *J. Fluid Mech.* **766**, 590 (2015).
- [16] M. A. Herrada and J. M. Montanero, A numerical method to study the dynamics of capillary fluid systems, *J. Comput. Phys.* **306**, 137 (2016).
- [17] A. G. Gaonkar, Interfacial tensions of vegetable oil/water systems: Effect of oil purification, *J. Am. Oil Chem. Soc.* **66**, 1090 (1989).
- [18] G. K. Batchelor, *An Introduction to Fluid Dynamics* (Cambridge University Press, Cambridge, 1967).
- [19] M. R. Khorrami, A Chebyshev spectral collocation method using a staggered grid for the stability of cylindrical flows, *Int. J. Numer. Methods Fluids* **12**, 825 (1991).
- [20] H. K. Moffatt, Viscous and resistive eddies near a sharp corner, *J. Fluid Mech.* **18**, 1 (1964).
- [21] V. Shtern, Moffatt eddies at an interface, *Theor. Comput. Fluid Dyn.* **28**, 651 (2014).
- [22] U. T. Bödewadt, Die drehströmung über festem grunde, *Z. Angew. Math Mech.* **20**, 241 (1940).
- [23] L. Carrión, M. A. Herrada, and V. N. Shtern, Instability of a water-spout flow, *Phys. Fluids* **28**, 034107 (2016).
- [24] T. von Kármán, Über laminare und turbulente Reibung, *Z. Angew. Math. Mech.* **1**, 233 (1921).